Supporting Information

Metallic Crystal with a Three-Dimensional Narrow Band Based on an Aromatic Hydrocarbon Derivative

Misako Ikeda, Yoshiki Sasaki, Yoshino Fujikawa, Shigeki Mori, Kensuke Konishi, Keishi Ohara, Haruhiko Dekura, Hiromichi Toyota, Masayoshi Takase, Ami Mi Shirai, Yuta Murotani, Ryusuke Matsunaga, and Toshio Naito

Contents

Crystal and molecular structures of neutral EtHAC

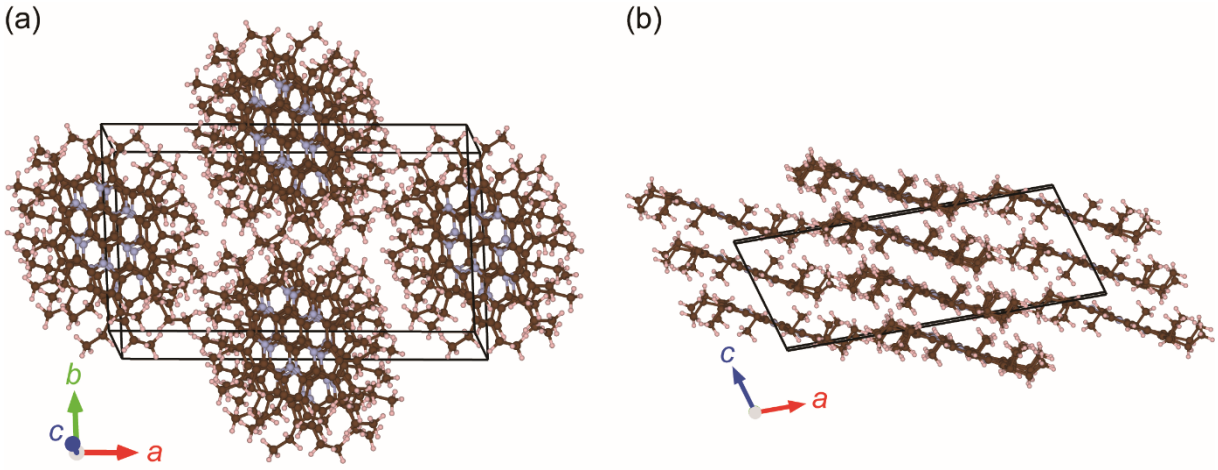

Figure S1. Crystal structure of neutral EtHAC at 100 K. View (**a**) down along and (**b**) perpendicular to the columns.[S1] Brown, purple, and pink spheres indicate C, N, and H atoms, respectively. Neutral EtHAC molecules form a columnar structure along the *c*-axis with a regular interplanar distance of 3.3168(18) Å.

To show how the delocalization of electrons in the frontier orbitals in EtHAC depends upon crystal structures and formal charges, we briefly review the molecular and crystal structures of neutral EtHAC.[S1] **Figures S1a**–**S1b** show the crystal structure of neutral EtHAC at 100 K, where the asymmetric unit contains a half of EtHAC molecule. As the ten ethyl groups play a dominant role in the cooperative properties such as electrical conductivity and magnetic susceptibility in $(EtHAC)_2I_3$, we will pay our attention to them in the discussion below. In the solid state of EtHAC, the neural molecules regularly stack to form a columnar structure along the [001]-direction with a repeating interplanar distance of 3.3168(18) Å. All methylene carbon atoms of the ethyl groups are coplanar with the aromatic skeleton, while all methyl groups are almost upright on either side of the aromatic skeleton. In solution, the ^{1}H- and ^{13}C-NMR spectra are like those in related compounds,[S2] indicating that all ethyl groups in isolated EtHAC molecules are in a standard electronic state, free of hyperconjugation. However, such an electronic state regarding delocalization changes in the solid states. The intermolecular interactions markedly induce hyperconjugation in $(EtHAC)_2I_3$.

Details of crystal structure of $(EtHAC)_2I_3$

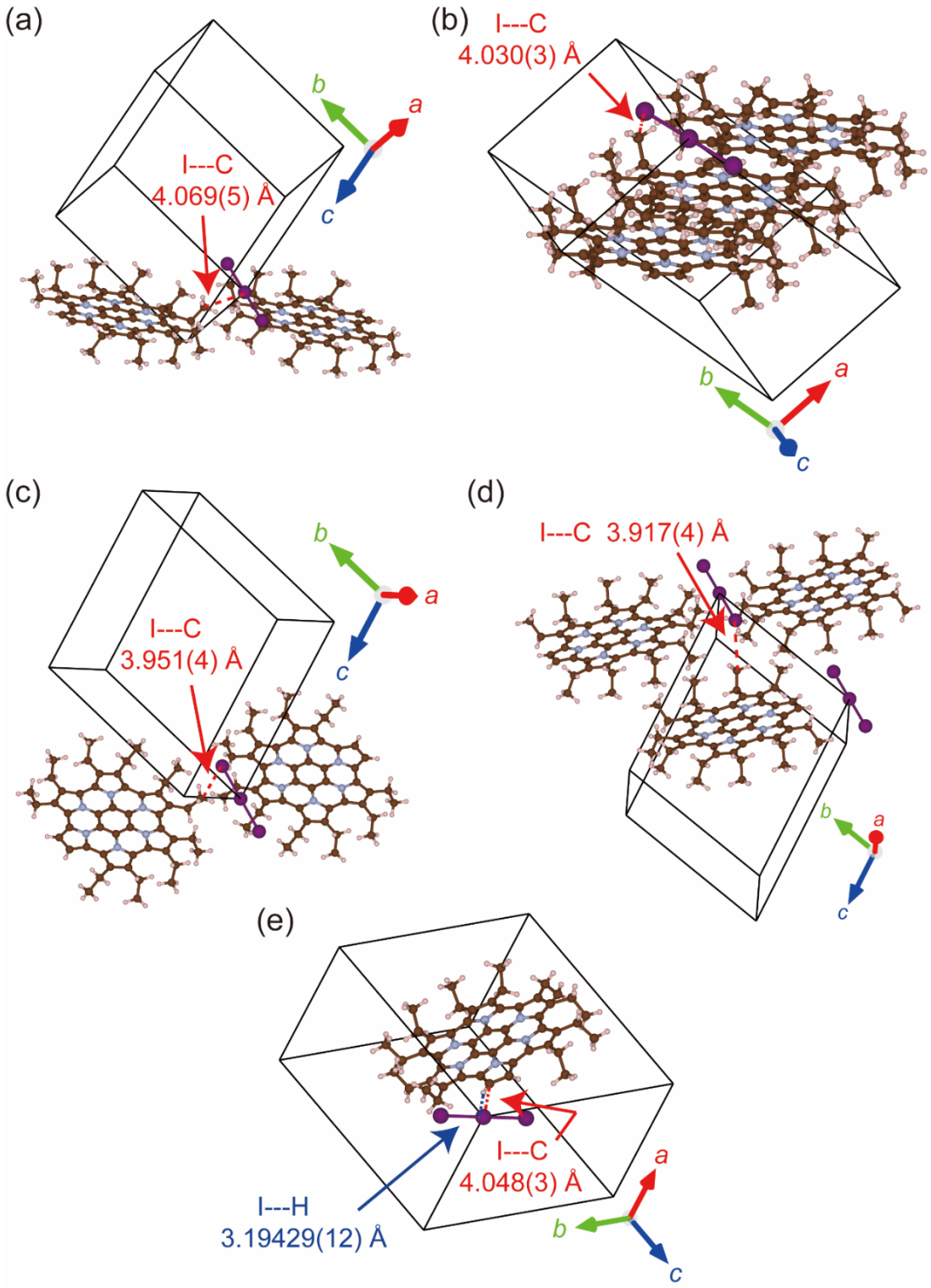

Figure S2. Selected interatomic I---C or I---H distances between EtHAC and I_3 species (Sample #31, 90 K). (**a**), (**b**), (**c**), and (**d**) Those involving C atoms in the ethyl groups. (**e**) Those involving C or H atoms in the pyrrole rings. (van der Waals radii) C (in CH_2 and CH_3): 2.00 Å, I: 2.15 Å, and H: 1.2 Å.[S3] Brown, pink, blue, and violet spheres designate C, H, N, and I atoms, respectively.

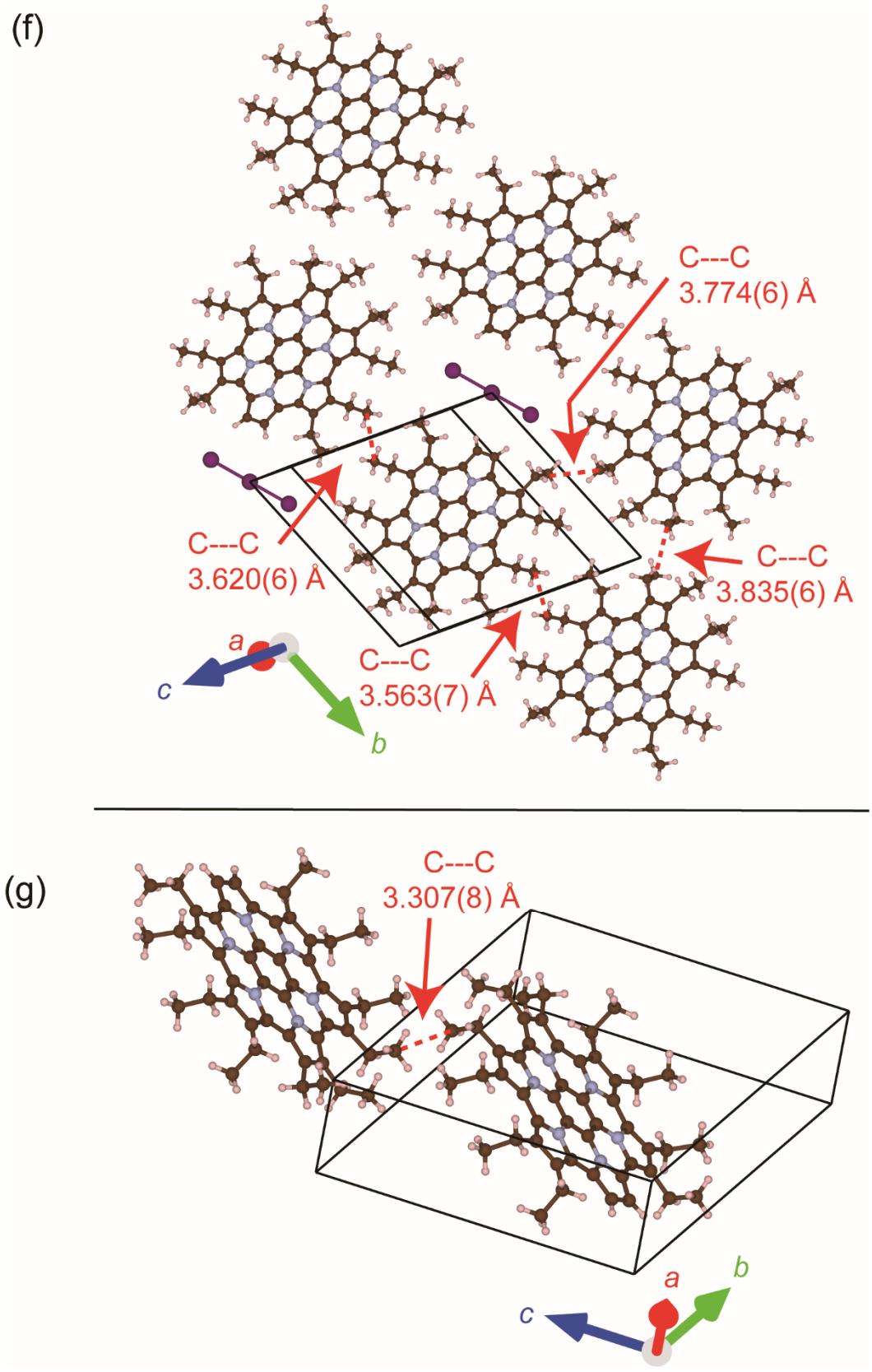

Figure S2 (Continued). (**f**) and (**g**) Selected intercolumnar C---C distances between ethyl groups in $EtHAC_2I_3$ (Sample #31, 90 K).

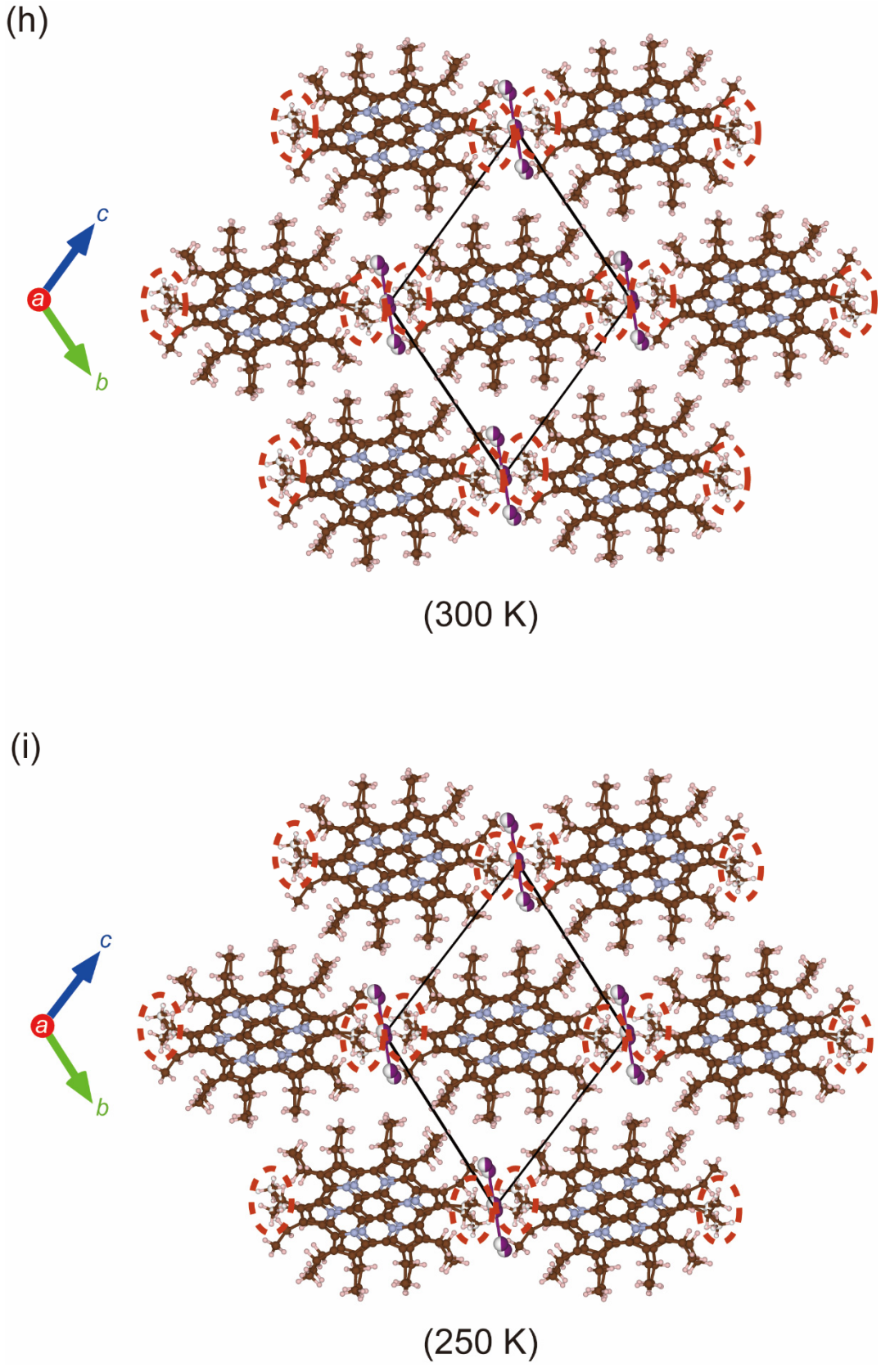

Figure S2 (Continued). Crystal structures of $EtHAC_2I_3$ (Sample #138) at (**h**) 300 K and (**i**) 250 K. The ethyl groups in red broken circles and all I_3 anions are disordered at 300 and 250 K.

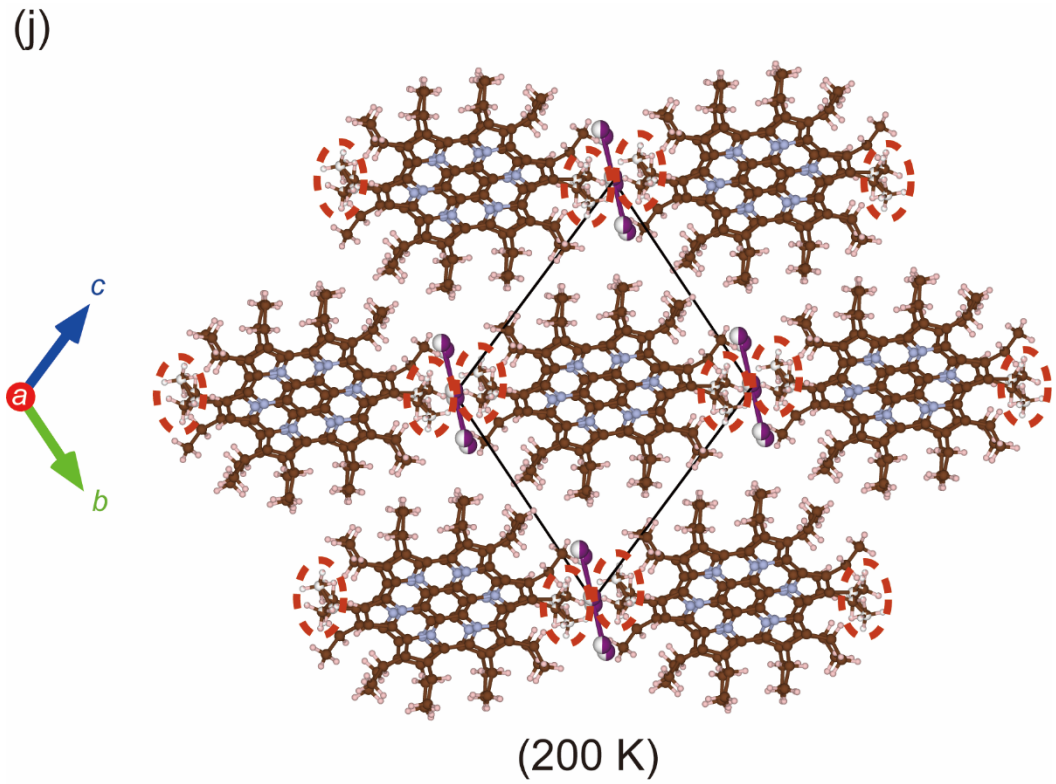

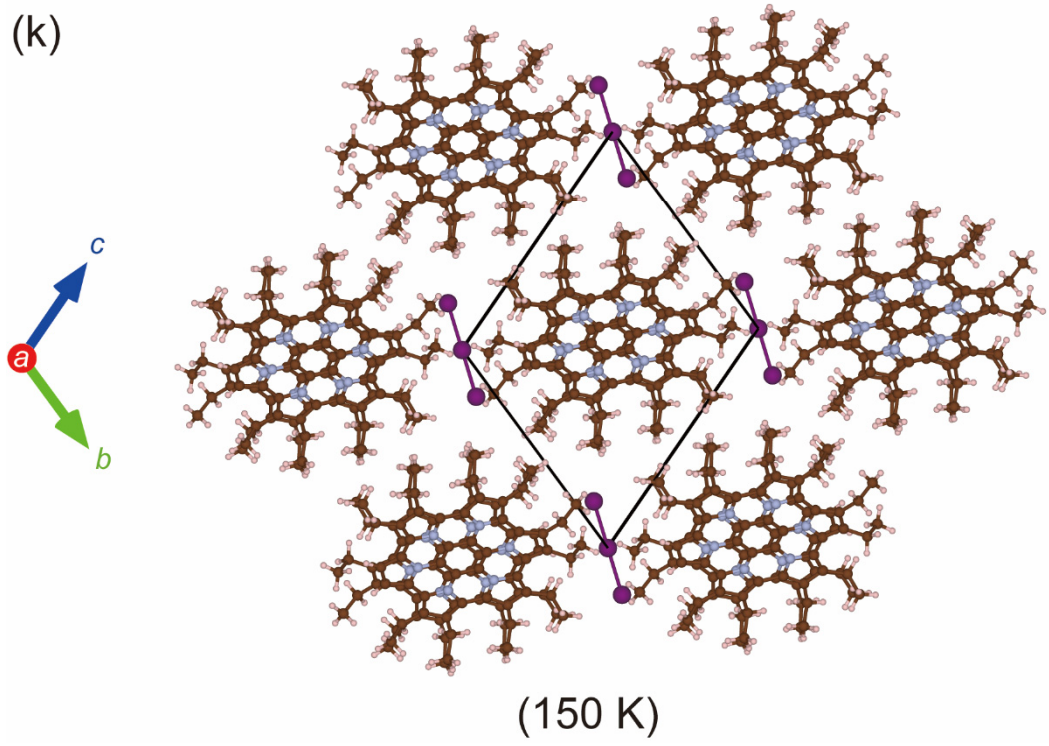

Figure S2 (Continued). Crystal structures of $EtHAC_2I_3$ (Sample #138) at (**j**) 200 K and (**k**) 150 K. The ethyl groups in red broken circles and all I_3 anions are disordered at 200 K, while they are ordered at 150 K.

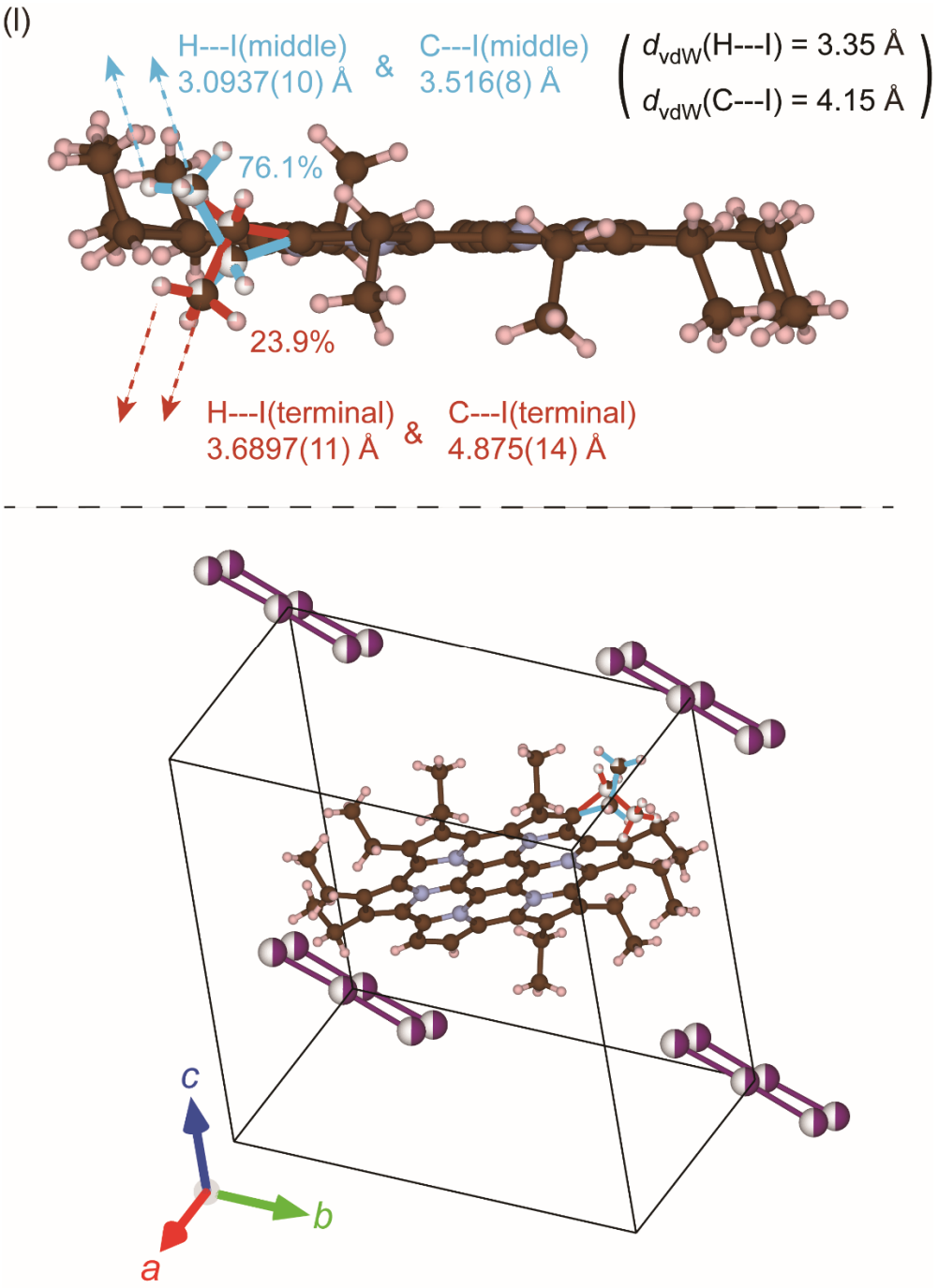

Figure S2 (Continued). Crystal structures of $EtHAC_2I_3$ (Sample #138). (**I**) Disorder of ethyl groups and I_3 anions (300 K): a close-up and side view of the EtHAC radical cation (upper) and a perspective of the unit cell (lower). The occupancy of positionally disordered I_3 anions are 50% each. The ethyl groups shown by blue and red bend upward (76.1%) and downward (23.9%) relative to the HAC plane, respectively. Both disorder patterns enable interatomic contacts between (-CH_2)-CH_3 group and I_3 anions. The terminal methyl groups in the major and minor ethyl conformations are closest to the middle and terminal I atoms in the nearest I_3 anions, respectively. The shortest interatomic H-I and C-I distances are 3.0937(10) and 3.516(8) Å for the major ethyl groups, respectively, and 3.6897(11) and 4.875(14) Å for the minor ethyl groups, respectively. The van der Waals distances d_{vdW} are 3.35 and 4.15 Å for H---I and C---I, respectively. These distances and ratio of the disorder patterns are summarized in Tables S1 and S2.

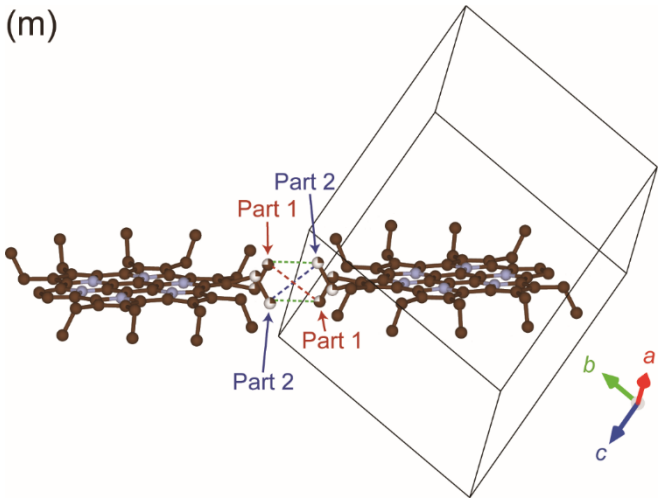

Figure S2 (Continued). Crystal structures of $EtHAC_2I_3$ (Sample #138). (**m**) Intercolumnar Et-Et contacts (300 K). Parts 1 and 2 designate the Et groups with major and minor occupancies in **Table S1**. H atoms are omitted for clarity.

Table S1. Interatomic contacts between Et groups and I_3^- ions (Sample #138).

T (K)	Occupancy Et group (%)	Occupancy I_3^- (%)[a)]	C---I (Å)[b)]	H---I (Å)[b)]
300	76.1	50	3.516(8), m	3.0937(10), m
	23.9	50	4.875(14), t	3.6897(11), m
250	71.5	50	3.527(7), m	3.0607(8), m
	28.5	50	4.806(11), t	3.7316(9), m
200	77.5	50	3.655(6), m	3.2131(11), m
	22.5	50	4.768(9), t	3.7788(12), m
150	(100)	(100)	3.976(5), t	3.55360(8), m
90	(100)	(100)	3.952(4), t	3.57153(8), m

[a)] Fixed values during the structural refinement, otherwise the least-square diverged.
[b)] The carbon atoms in the methyl groups in Et groups. The letter m and t indicate the middle and terminal I atoms in the nearest I_3 anions, respectively.

Table S2. Intercolumnar Et-Et contacts (Sample #138). Parts 1 and 2 designate the Et groups with major and minor occupancies in **Fig. S2m** and **Table S1**.

T (K)	C(Part 1)---C(Part 2) (Å)	C(Part 1)---C(Part 1) (Å)	C(Part 2)---C(Part 2) (Å)
300	3.434(13)	4.107(11)	3.83(3)
250	3.366(11)	4.043(10)	3.78(3)
200	3.310(10)	3.959(8)	3.71(3)
150	NA	3.876(7)	NA
90	NA	3.861(6)	NA

Table S3. Interatomic distances (I—I) in polyiodide monoanions and related species.

Compounds	I-I distances (Å)	I-I-I angles (°)	*T* (K)	references	CCDC #
I_2 (solid)	2.715	N.A.	110	S3	N.A.
$(n\text{-}C_4H_9)_4NI_3$[b]	2.9371(6), 2.9070(6)	174.726(18)	293	This work	2405509
	2.9491(6), 2.8848(6)	178.450(19)			
$(EtHAC)_2I_3$[b]	2.9235(19), 2.9124(18)	176.84(6)	300	This work	2394976
	2.9238(15), 2.9178(15)	177.07(5)	250	This work	2394977
	2.9250(16), 2.9160(15)	176.88(6)	200	This work	2394978
	2.9308(5), 2.9307(5)	180.0	150	This work	2394979
	2.9322(3), 2.9321(3)	180.0	90	This work	2394981
$(EtHAC)_2I_3$[c]	2.9296(3)	180.0	90	This work	2350026

[a] Crystallographically independent two symmetric I_3^- species.

[b] Crystallographically unique asymmetric I_3^- species.

[c] Crystallographically unique and only symmetric I_3^- species.

Calculated electronic structures of $(EtHAC)_2I_3$

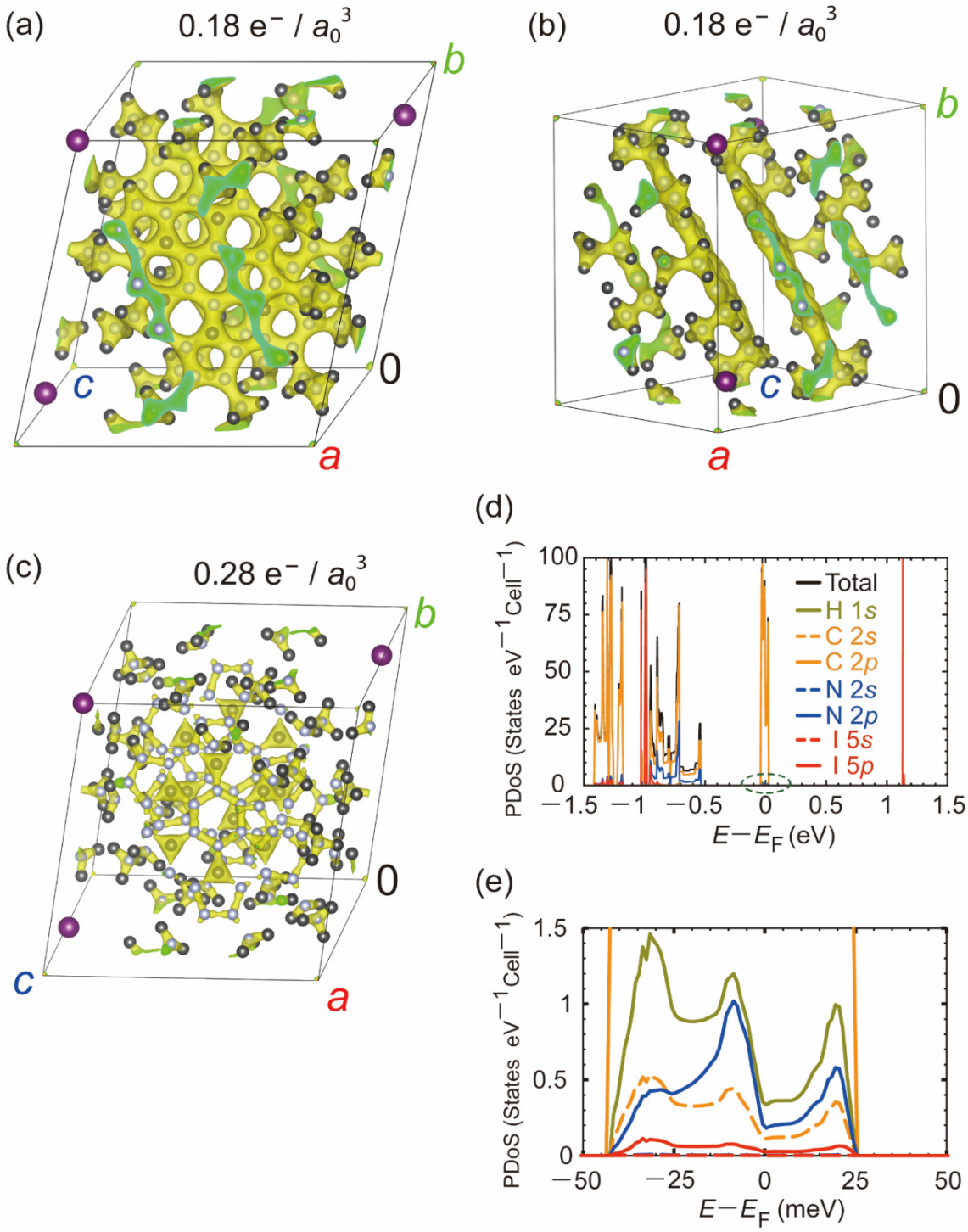

Figure S3. Calculated electronic structures of $(EtHAC)_2I_3$ based on a DFT method and the observed atomic parameters at 90 K (Sample #31). (**a**), (**b**), and (**c**) Charge densities described as isosurface of the value indicated above each panel, where a_0 indicates the Bohr radius. Green sections are those truncated by the faces of the unit cell. (**a**) and (**b**) show the identical isosurface viewed from different angles. (**d**) and (**e**) Projected density of states by the unit of (States eV^{-1} $Cell^{-1}$). (**e**) shows an enlarged view of the part in the broken circle in (**d**).

Electrical behavior of $(EtHAC)_2I_3$

We will make a brief comment on the relationship between structural and physical properties in terms of disorder of the ethyl groups. When the material was rapidly cooled ("fast-cooling", not slower than –1 K/min), $(EtHAC)_2I_3$ exhibited insulating behavior (**Figure S4h**). The resistivity was higher than the metallic state by three orders of magnitude or more with evidently non-metallic *T*-dependence ($d\rho/dT < 0$). Yet, the *T*-dependence did not match the Arrhenius-type behavior ($\log\rho \propto 1/T$), implying that the non-metallic behavior with quite high resistivity should originate from a different cause from a band gap. Additionally, the same single crystal once exhibited metallic behavior when it was slowly cooled as described below (**Electrical resistivity measurements**), and then exhibited insulating behavior when it was rapidly cooled (–1 K/min from 300 to 2 K: Compare **Figures S4h** and **S4i**).

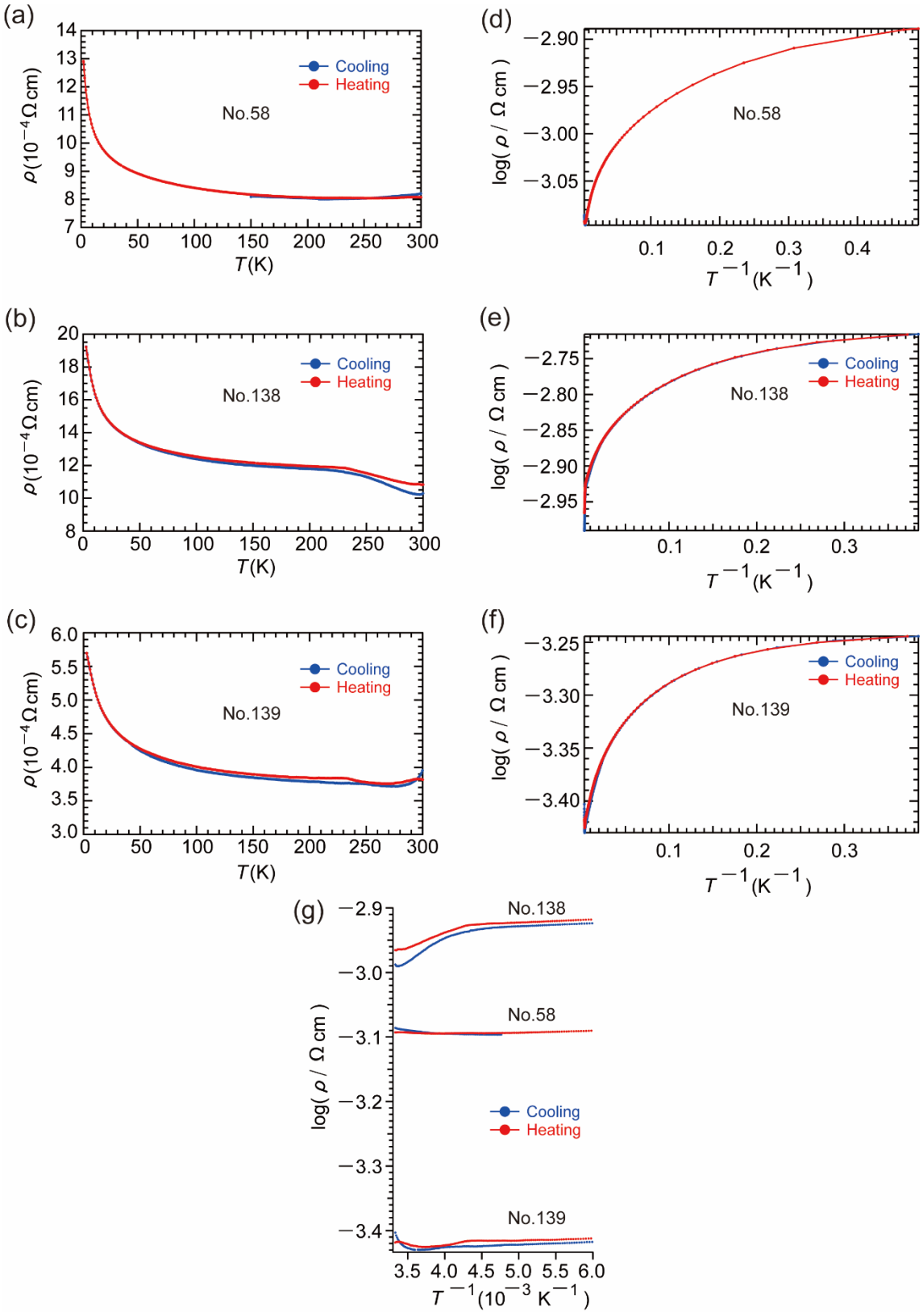

Figure S4. Electrical resistivity measured by a standard four-probe method using the single crystal and direct current along the *a*-axis. The same data in **Figure 3** of (**a**) Sample #58, (**b**) Sample #138, and (**c**) Sample #139. Arrhenius plot of the same data of (**d**) Sample #58, (**e**) Sample #138, and (**f**) Sample #139. (**g**) Enlarged view of the higher temperature range (~170—300 K) of Figures S4d—S4f. Red and blue dots indicate the data obtained in heating and cooling processes, respectively.

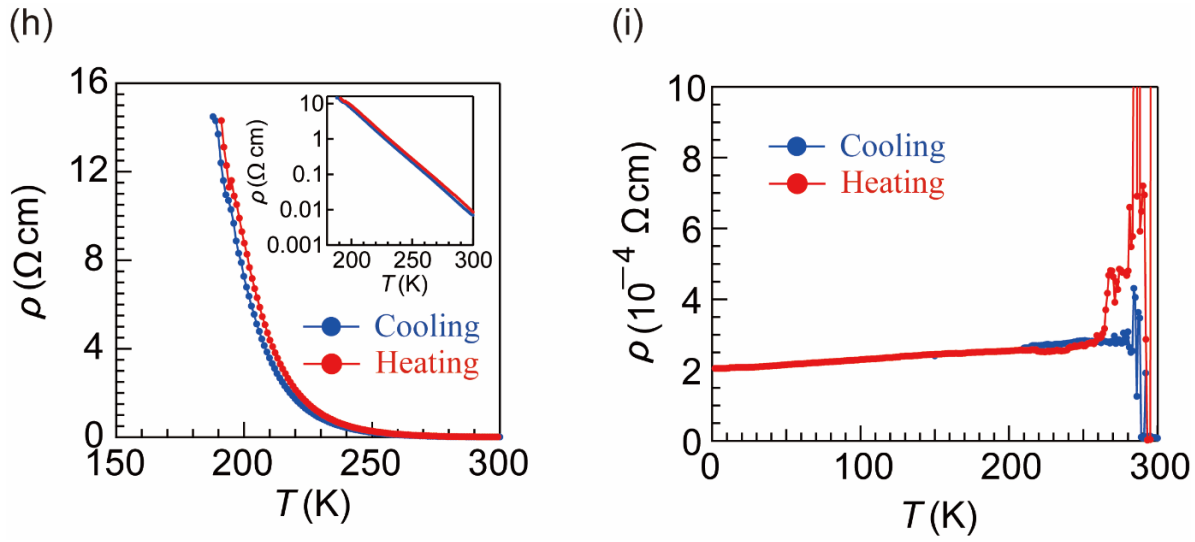

Figure S4 (Continued). Electrical resistivity measured by a standard four-probe method using the single crystal (Sample #59) and direct current along the *a*-axis. (**h**) –1 K/min, and (**i**) –0.1 K/min (300—260 K), –0.2 K/min (260—210 K), –0.3 K/min (210—150 K), and –1 K/min (150—2 K). Heating rate (2—300 K) was 2 K/min in both measurements. The electrical behavior was transformed from the metallic (i) to the insulating (h) properties by changing the cooling rates in the same measurement using the same single crystal. The measurement was carried out under the identical conditions with the data shown in **Figure 3**, except for the cooling rates. Red and blue dots indicate the data obtained in heating and cooling processes, respectively.

Raman spectra of $(EtHAC)_2I_3$

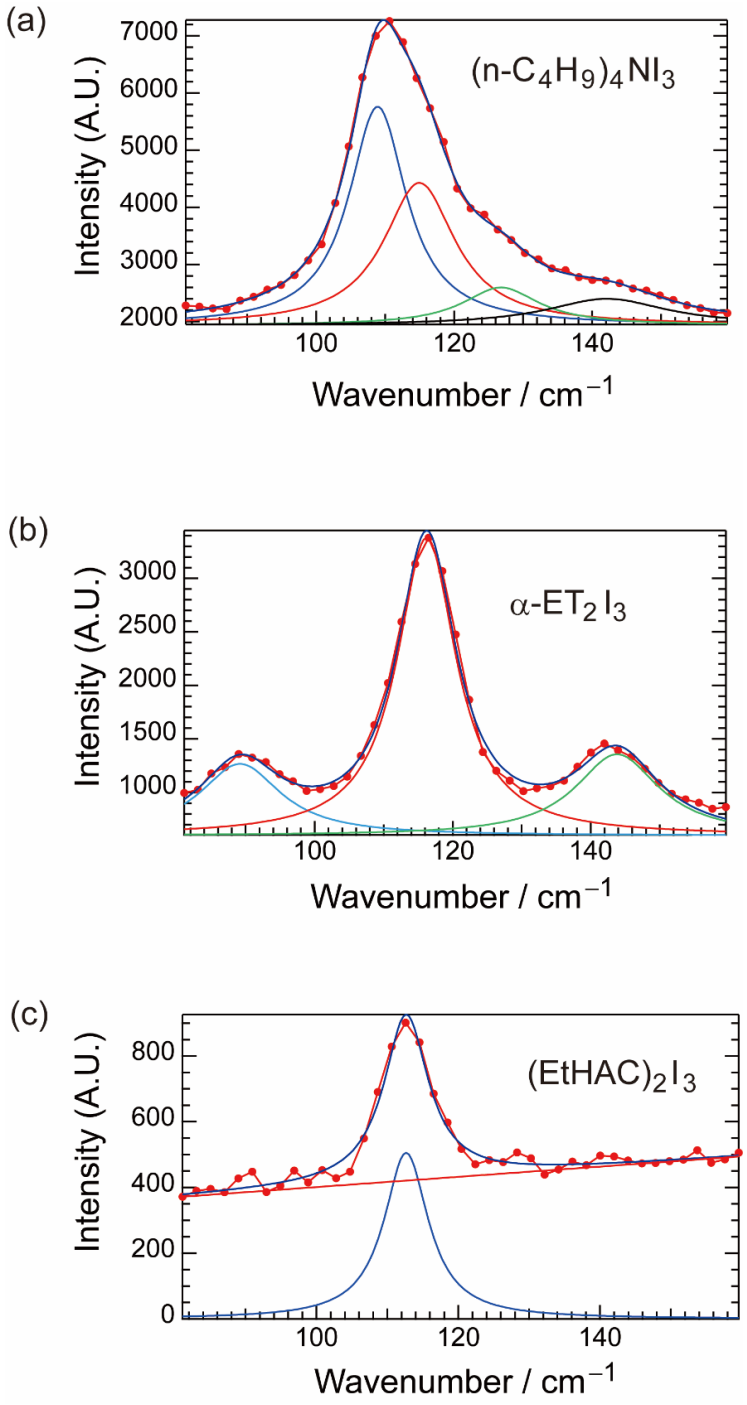

Figure S5. Raman spectra of I_3 anions. The observed spectra (red closed circles and lines) and best-fit curves (dark blue curves) are shown. Symmetrical stretch vibration (ν_1) and other vibration modes of (a) $(n\text{-}C_4H_9)_4NI_3$, (b) $\alpha\text{-}ET_2I_3$, and (c) $(EtHAC)_2I_3$. In Figs. S5(a) and S5(b), also shown are deconvoluted peaks obtained from curve-fitting analyses (for details, see Table S3). In Fig. S5(c), the corrected baseline (red) and the best-fit curve based on the corrected baseline (blue, lower spectrum) are also shown.

Table S4. Curve-fitting analyses of the Raman spectra (Figure S5).[a)]

Compounds	Peak 1 (cm^{-1})	Peak 2 (cm^{-1})	Peak 3 (cm^{-1})	Peak 4 (cm^{-1})
$(n\text{-}C_4H_9)_4NI_3$	108.91	114.96	126.78	142.13
$\alpha\text{-}ET_2I_3$[b)]	116.23	N.A.	N.A.	N.A.
$(EtHAC)_2I_3$	112.65	N.A.	N.A.	N.A.

a) Considering the number of independent vibration modes of I_3^- anions in the asymmetric unit, the peak profile of $(n\text{-}C_4H_9)_4NI_3$ spectrum was deconvoluted into four Lorentzian oscillators, while a single Lorentzian oscillator was assumed for each of the remaining two compounds. Only the deconvoluted peaks assigned to ν_1 are shown in Table S3.

b) ET = bis(ethylenedithio)tetrathiafulvalene. The DFT calculation of the band structure of $\alpha\text{-}ET_2I_3$ was reported in a previous study,[S4] while the Raman spectrum was acquired in this study. The first-principles (VASP) band structure indicated strong CT interaction between ET and I_3 species.

Electron spin resonance of $(EtHAC)_2I_3$

Table S5. Best-fit parameters for reproducing the observed angle-dependence of ESR.[a]

Rotation Angles	Properties	y_0	A_1	f_1	c_1 (°)	A_2	f_2	c_2 (°)
θ	Γ	66.9 (μT)	7.31 (μT)	0.070	98	3.42 (μT)	0.0358	168
ϕ	Γ	69.1 (μT)	0.74 (μT)	0.110	296	13.4 (μT)	0.0350	149
θ	g-value	1.99841	5.36×10^{-5}	0.018	102	1.64×10^{-4}	0.035	181
ϕ	g-value	1.99817	6.15×10^{-5}	0.017	–8	9.37×10^{-5}	0.036	240
θ	I	14.50201	0.45047	0.07010	4.74027	0.30154	0.02778	2.69266
ϕ	I	14.65455	0.11796	0.06918	2.64068	0.79977	0.03488	–0.42642

[a] Sample #156. Trial function for the fitting is as follows.

$$f(x) = y_0 + A_1 \sin(f_1 x + c_1) + A_2 \sin(f_2 x + c_2)$$

(a)

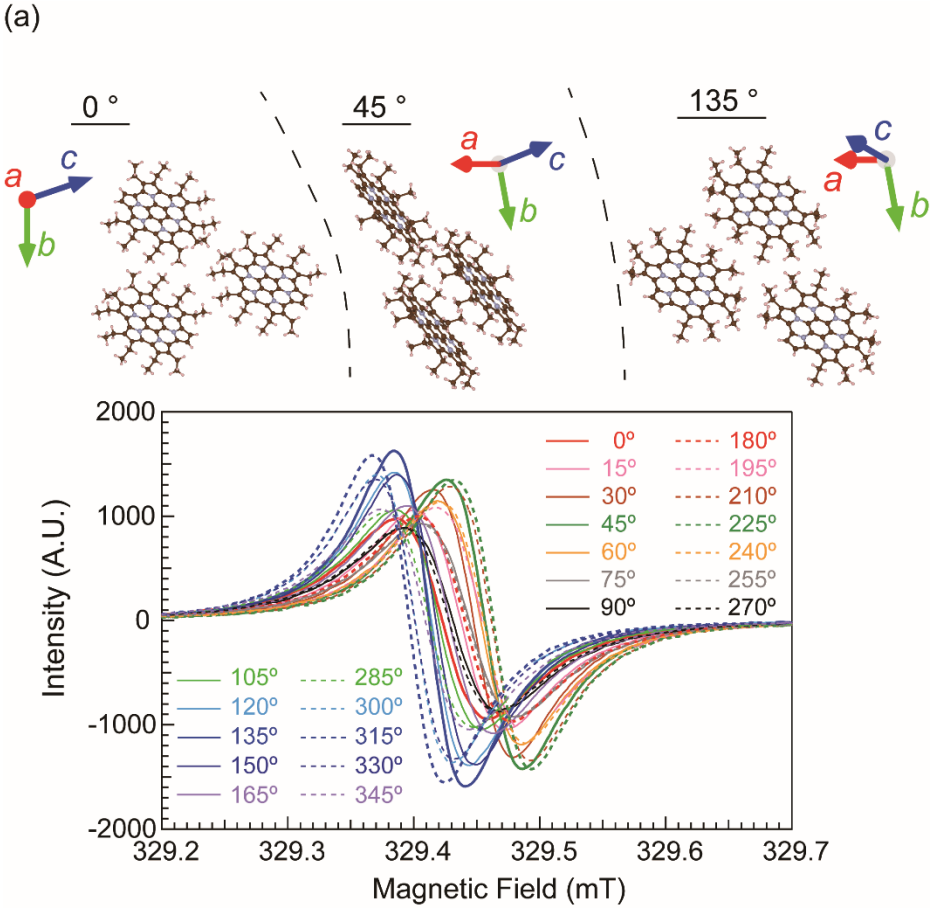
0 °
45 °
135 °
a
c
b
Intensity (A.U.)
Magnetic Field (mT)
0°
15°
30°
45°
60°
75°
90°
105°
120°
135°
150°
165°
180°
195°
210°
225°
240°
255°
270°
285°
300°
315°
330°
345°

(b)

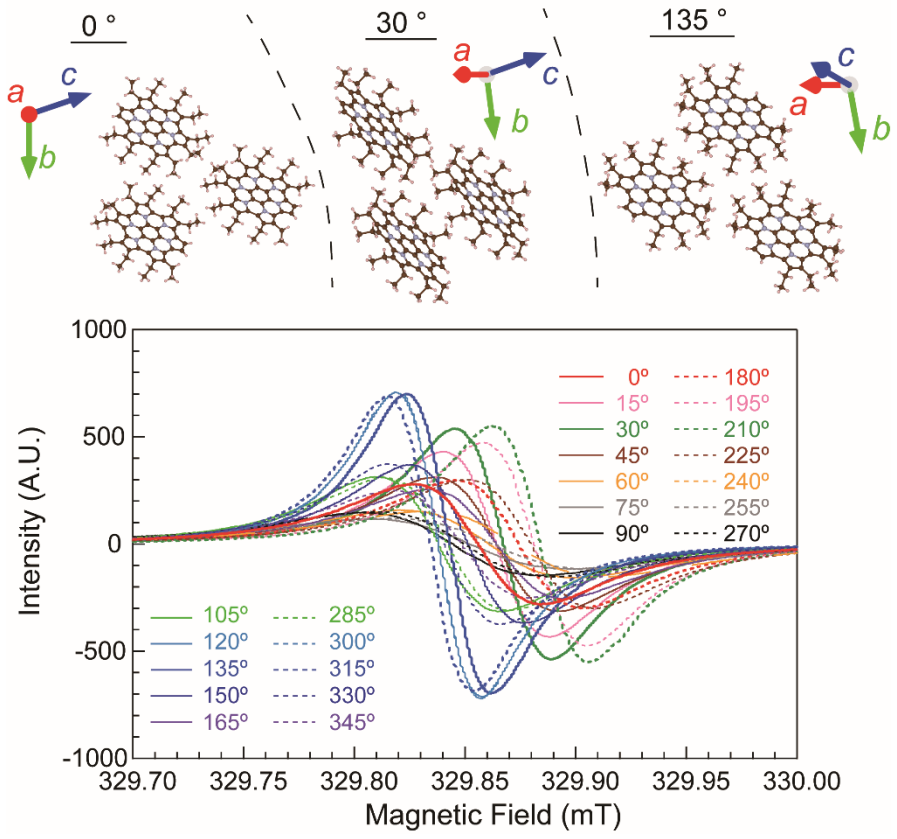
0 °
30 °
135 °
a
c
b
Intensity (A.U.)
Magnetic Field (mT)
0°
15°
30°
45°
60°
75°
90°
105°
120°
135°
150°
165°
180°
195°
210°
225°
240°
255°
270°
285°
300°
315°
330°
345°

Figure S6. ESR spectra of $(EtHAC)_2I_3$ measured using single crystals at 296 K. The indicated angles are θ. (a) Metallic (Sample #156) and (b) insulating (Sample #3) samples. All spectra in (a) and (b) were measured using the same single crystals, respectively. Note the smaller anisotropy in intensity in the metallic sample than that of the insulating sample.

Experimental Details

Materials

All the chemical reagents were purchased as purest grades and used without further purification. Dry solvents were purchased from FUJIFILM Wako Pure Chemical Corporation.

$(EtHAC)_2I_3$

EtHAC (2 mg, 2.7×10^{-3} mmol)[S1] was dissolved in C_6H_5Cl (0.5—0.7 mL) in a small brown vial (No. 02, 2.2 mL, As One). Iodine (24 mg) was dissolved in C_6H_5Cl (10 mL) using an ultrasonic cleaning machine, and 0.21 mL of the solution (0.5 equivalent as I_3^- anions required for 0.5-electron-oxidation) was added to the EtHAC solution by a disposable syringe. The vial was placed without a seal in a larger brown vial (No. 07, 50 mL, As One), which contained the mixed solvent of C_6H_5Cl:hexane =1:1—1:3 (~2 mL). The larger vial was loosely sealed to allow spontaneous vaporization and emission of volatile components to surroundings, during which the inner solution of EtHAC was slowly diluted by the vapor of the outer mixed solvent (mainly, hexane). By intermittent addition of a small amount of hexane to the outer solvent, thick black needles were obtained after 3—4 days. The crystals were filtered and washed with hexane with suction. The obtained products often contained single crystals of different stoichiometries including $EtHAC^+$ and/or $EtHAC^{2+}$ species and C_6H_5Cl molecules.

Single crystal X-ray structural analyses

Details of the single crystal X-ray structural analyses are described in our previous paper.[S5] The single-crystal X-ray structural analyses were performed using VariMax SaturnCCD724α (Rigaku, Tokyo, Japan) with a temperature controller of a continuous-flow-type liquid nitrogen cryostat. The analyses were performed at 300, 250, 200, 150, and 90 K using the single crystals of $EtHAC_2I_3$ examined in advance by the X-ray oscillation photographs, electron spin resonance, and temperature-dependence of electrical resistivity for relating the structure and properties of each crystal. The structural analyses at different temperatures were performed using different single crystals with clear metallic properties, which demonstrated good reproducibility and practically no sample dependence. To present the reproducibility and sample dependence, we present the crystal structures and the corresponding properties of different single crystalline samples in this paper with indicating the sample numbers. The effects of the cooling rate on the structures were examined using rapid (–1.0 K/min) and slow (–0.1 K/min) cooling processes from 298 to 90 K. The collected data were processed using CrysAlisPro ver. 171.41_64.93a (Rigaku, Tokyo, Japan) prior to the structure solving and refinement using Olex 2-1.5. The hydrogen atoms were located at the calculated positions when the ethyl

groups were not disordered; otherwise, they were located using difference Fourier syntheses. Further details of the data collection and analyses are described in the .cif files deposited to the Cambridge Crystallographic Data Centre (CCDC# 2394976 (300 K, #138), 2394977 (250 K, #138), 2394978 (200 K, #138), 2394979 (150 K, #138), 2394981 (90 K, #138), and 2350026 (90 K, Sample #31)). The obtained structures at 90 K from #138 and #31 agreed with each other within experimental error (esd's).

First-principles band structure calculations

We performed the density-functional theoretic calculations[S6,S7] within the local density approximation[S8,S9] for the $(EtHAC)_2I_3$ using the crystal structure experimentally assigned at 90 K (Sample #31). Scalar relativistic corrections were included to account for relativistic effects on core electrons. The valence electron wavefunctions were pseudized based on the ultrasoft pseudo potential scheme.[S10] The electron configurations for the pseudopotentials of H, C, N, and I were treated as ($1s^1$), ($2s^2$ $2p^2$), ($2s^2$ $2p^3$), and ($5s^2$ $5p^5$), respectively. The 70 and 320 Ry cutoffs for kinetic energy and charge density were applied to all the calculations. A 4 × 4 × 2 ***k***-points uniform grid was sampled in the first Brillouin zone for the self-consistent field (SCF) electronic structure calculations. Projected density of states (DoS) and Fermi-surface were obtained with detailed electronic structure calculated by the non-SCF calculations with a much denser mesh of uniform 12 × 12 × 8 points. We confirmed that these calculation conditions produced sufficient convergences in Fermi energy (< 0.5 meV) and total DoS at the level (< 0.4 States eV^{-1} $cell^{-1}$), respectively. The temperature effect on the electronic structure was considered by applying the Fermi-Dirac smearing to the electronic configurations at the ground state. All the calculations were carried out using the QUANTUM ESPRESSO distribution[S11].

Electrical resistivity measurements

The details of measurement procedure are reported in our previous paper.[S5] The crystals are needles developed along the *a*-axis. The crystals were freshly grown and filtered, and the electrical contacts were made with gold wires (0.015 mm in thickness; The Nilaco Corp., Tokyo, Japan) and carbon paste (DuPont Japan, Tokyo, Japan) immediately before the measurements. The measurements (2—300 K) were carried out in a reduced pressure of He atmosphere on the single crystals by a four-probe method. The constant current (100 μA) was along the crystallographic *a*-axis or the direction indicated in the data. The equipment was Physical Property Measurement System PPMS-9 (Quantum Design). The cooling rates were –0.1 K/min (300—260 K), –0.2 K/min (260—210 K), –0.3 K/min (210—150 K), and –1 K/min (150—2 K), while the heating rate was +2 K/min at 2—300 K.

Raman spectra measurements

Raman spectra were measured using a Renishaw inVia Raman microscope Reflex at 296 K and the single crystals. The crystallinity and the directions of *a*-, *b*-, and *c*-axes relative to the outline of each specimen were checked by the X-ray oscillation photographs prior to the Raman measurements to select high quality single crystals. The samples were fixed on a slide glass of optical-grade quartz (hight 26 × width 76 × thickness 1.5 mm^3, Fujiwara Scientific Co., Ltd) with a minimum amount of grease. Then, the slide glass was set in the sample room of the spectrometer to align the averaged directions of the long molecular axes of I_3^- anions being parallel with the polarization angle of the incident beam as much as possible. The objective lens was ×20 or ×50, depending upon the sample dimensions. The spectral and spatial resolutions were 0.3 cm^{-1} (FWHM), 1.6 μm (×20) and 865 nm (×50) for lateral resolution, and 6.7 μm (×20) and 1.9 μm (×50) for axial resolution, respectively. The excitation wavelength was 532 nm (150 mW, Nd:YVO_4, JUNO, Kyocera SOC Corporation) and the laser power during the measurements was attenuated to 0.05% of the full power. Since prolonged or intense laser irradiation of ~530 nm beam was reported to decompose the polyiodide anions,[S12] we checked that the obtained spectra did not contain impurity peaks due to decomposition such as I_5^- ($I_5^- = I^- \cdot 2I_2$, exhibiting Raman peaks at 143 and 165 cm^{-1}) and the reproducibility. We also checked (in)homogeneity of the samples by measuring different points on the same single crystals, which gave identical spectra except for signal intensities, as they were sensitive to the surface roughness and incident angles.

Electron spin resonance measurements

The details of measurement and analysis are reported in our previous paper.[S13] The measurements were carried out using JEOL JES FA100 (X-band spectrometer; 9.3 GHz) at 296 K. The single crystal (~0.55 × 0.04 × 0.04 mm^3) was mounted on a Teflon piece with a minimum amount of MOLYKOTE high vacuum grease (Dupont) in a quartz sample tube. The background signals were measured prior to the sample measurement under conditions identical to those of the samples, and the resultant spectra were subtracted from the raw sample spectra. The microwave power, *Q*-values, time constant, sweep time, modulation, and modulation width were 1 mW, 7000—9500, 0.03 s, 30 s, 100 kHz, and 0.01 mT, respectively. The magnetic field was corrected by a Gauss meter (JEOL NMR Field Meter ES-FC5) at the end of every measurement and was doubly checked by a standard sample (colourless powder of a Mn(II) compound dispersed in ZnO powder). For anisotropy measurements in both θ- and ϕ-rotation patterns, the single crystals were rotated clockwise when one looks down on the rotation axis. The origins of rotation angles are defined as the magnetic field $H \perp ab$ plane with setting the *a*-axis horizontal for $\theta = 0$ and $H \,//\, ab$ plane with setting the *a*-axis vertical (*i.e.* *a*-axis = the rotation axis) for $\varphi = 0$. All spectra were analysed by the spectral simulation to derive each *g*-value,

intensity I, and linewidth Γ, which was carried out using Anisotropic Simulation software AniSim/FA ver. 2.2.0 by JEOL.

Polarized infrared reflectance spectra measurements

The polarized reflectance spectra were measured using a spectrophotometer JASCO FT/IR-6600 (type A) equipped with a microscope IRT-5200 over the wavenumber region of 600—7800 cm^{-1}. The spectral resolution was 4 cm^{-1}. Every spectrum was accumulated by a hundred times to gain S/N. The detector was MCT cooled with liquid N_2. The sample temperature was controlled using a continuous He-flow-type cryostat Oxford Instruments MicrostatHe-R with a KRS-5 optical window. The incident and reflected light intensity loss by passing through the optical window of the cryostat was estimated by comparing the spectra measured with and without using cryostat. The loss was negligible and did not require correction. To avoid inducing and freezing ethyl group disorder, the sample was cooled with 1 K/min from 294 to 6.8 K. To compare the results, a different sample was cooled with different cooling rates: 1 K/min from 294 to 100 K and 2 K/min from 100 to 6.8 K. The spectra of different samples under different cooling conditions quantitatively gave identical results at the same temperature and the polarization angle within experimental error. The temperature fluctuation during the measurements was approximately within ± 0.01 K. The measurement temperatures were 294 K, 250 K, 200 K, 150 K, 100 K, 50 K, and 6.8 K, considering behaviour and anomalies observed in the resistivity. As hysteresis was observed in the temperature dependence of resistivity, the hysteresis of the spectra was examined by measuring them at 100 K, 200 K, and 294 K in the heating process from 6.8 K by the heating rate of 2 K/min (**Figures S7a—S7c**). For gaining most intense reflectance signal, an aperture for the reflected light was adjusted as large as possible within the crystal faces, which inevitably included rough surface parts in the beam spot. This technical limitations in setting the samples produced interference noise in some spectra. As the obtained spectra of 5500—7800 cm^{-1} were seriously noisy, they were not shown in the results (**Figures 5a** and **5b**). Various types of smoothing were attempted, yet the results depended on the type of smoothing too much to select the appropriate result without arbitrariness. Although vibration peaks might appear with possible noise peaks at ≤ 700 cm^{-1}, we present all spectra without smoothing. The samples were set on a gold-evaporated copper plate (*ca.* 1 cm × 1 cm, 0.3 mm thick). The copper plate was fixed on the cold head of the oxygen-free copper stage in the cryostat. The sample stage could be finely moved in the x-, y-, z-, and θ- directions for adjusting the focus and incident angle of the IR beam on the crystal faces but could not be adjusted in the remaining elevation and depression angle ϕ. Thus, to secure the normal incidence, we set the samples on the copper plate so as to place their crystal faces up as accurately as possible ($\sim \pm 10^{o}$) with a minimum amount of Apiezon N grease under the optical microscope (×20—40). These technical limitations in setting the samples could lower the absolute values of reflectance by ~10—20% at most. The optical system

for focus in the microscope IRT-5200 was based on a ×10 Cassegrain reflector, which makes the polarization ill-defined compared with other optical focussing methods. Still, it enabled qualitative discussion such as anisotropy but did not enable quantitative discussion such as the Kramers-Kronig analysis. The samples of the reflectance spectra were the single crystals of needles with irregular hexagonal sections. The suitable single crystals were selected based on the X-ray oscillation photographs showing high single crystallinity. Then, the selected crystals were further examined by resistivity measurements to select those retaining metallic behaviour at 300—2 K in a 3D manner, which was like those in Figures 3a—3d. The X-ray oscillation photographs were also used to identify the crystallographic axes for setting the polarization angles. The relative angles between the *a* axis and the longest dimension of the single crystals slightly differ from crystal to crystal (**Figure S8**). The *b* and *c* axis were not in the planes of the crystal faces in many crystals, making an angle of ~10—20^{o} with crystal faces. Considering all abovementioned factors, the error of the polarization angle was ~$\pm$5^{o} in the azimuthal and ~$\pm$10^{o} in the normal directions of the crystal face. The absolute values of reflectance were estimated measuring the reflectance of the evaporated gold mirror on the copper plate under the identical measurement conditions, which were measured for every spectrum with those of samples. To confirm the reproducibility and sample dependence we compared two independently measured spectra with *a* axis polarization, i.e., the spectrum of the crystal A (the *ab* plane) and that of crystal D (the *ac* plane). They agreed quantitatively with each other at all temperatures of measurement. Intense CO_2 peaks at 2300—2380 cm^{-1} were removed from the obtained spectra, which were interpolated between 2300—2380 cm^{-1}.

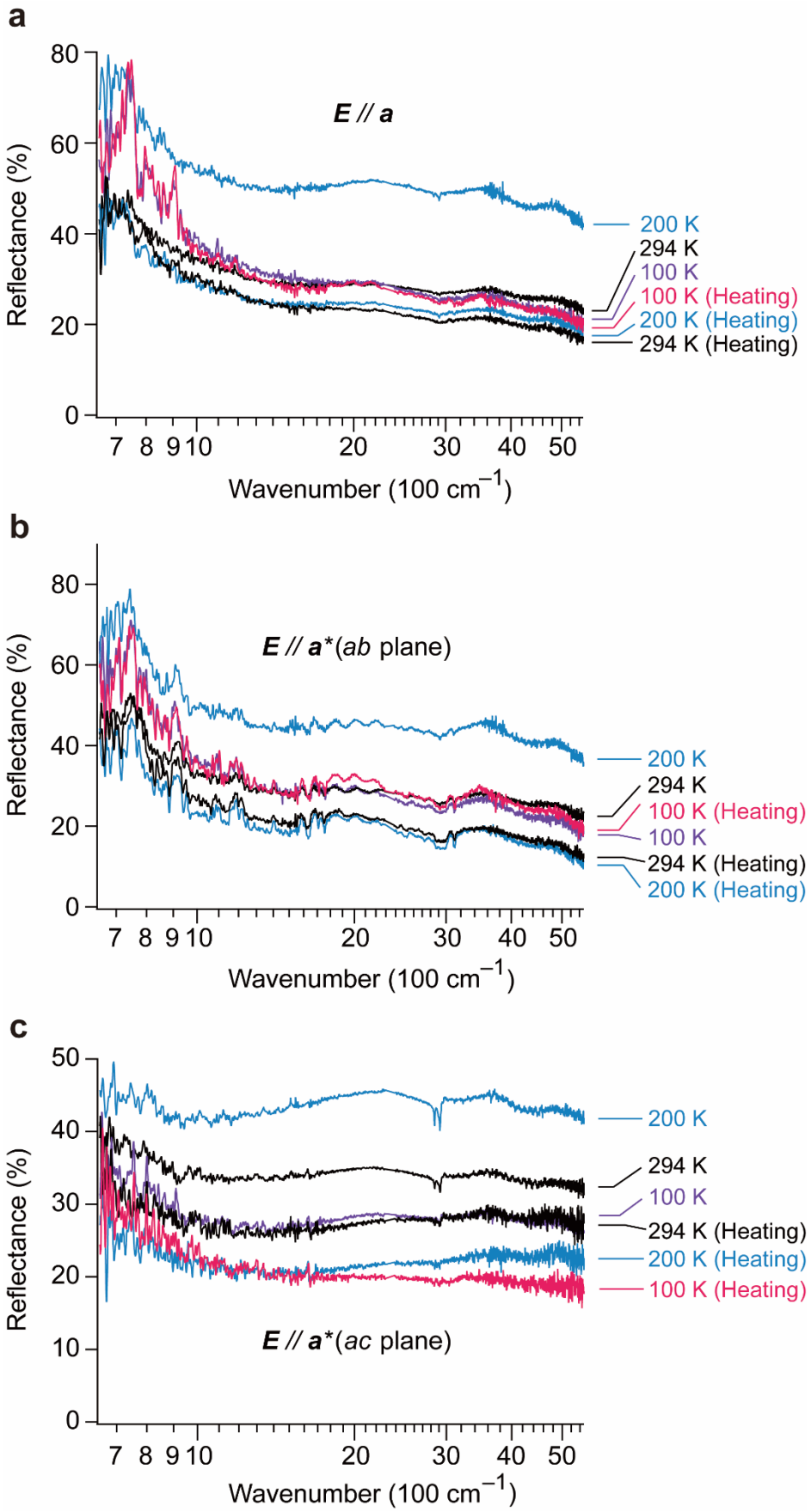

Figure S7. Hysteresis in the temperature dependence of reflectance spectra with polarization angles (a) //*a*, (b) //*a**(*ab*), and (c) //*a**(*ac*). Firstly, the spectra were measured in the cooling process from 294 to 6.8 K, then measured in the heating process from 6.8 to 294 K. For simplicity, only heating process is explicitly described in parentheses in the figures.

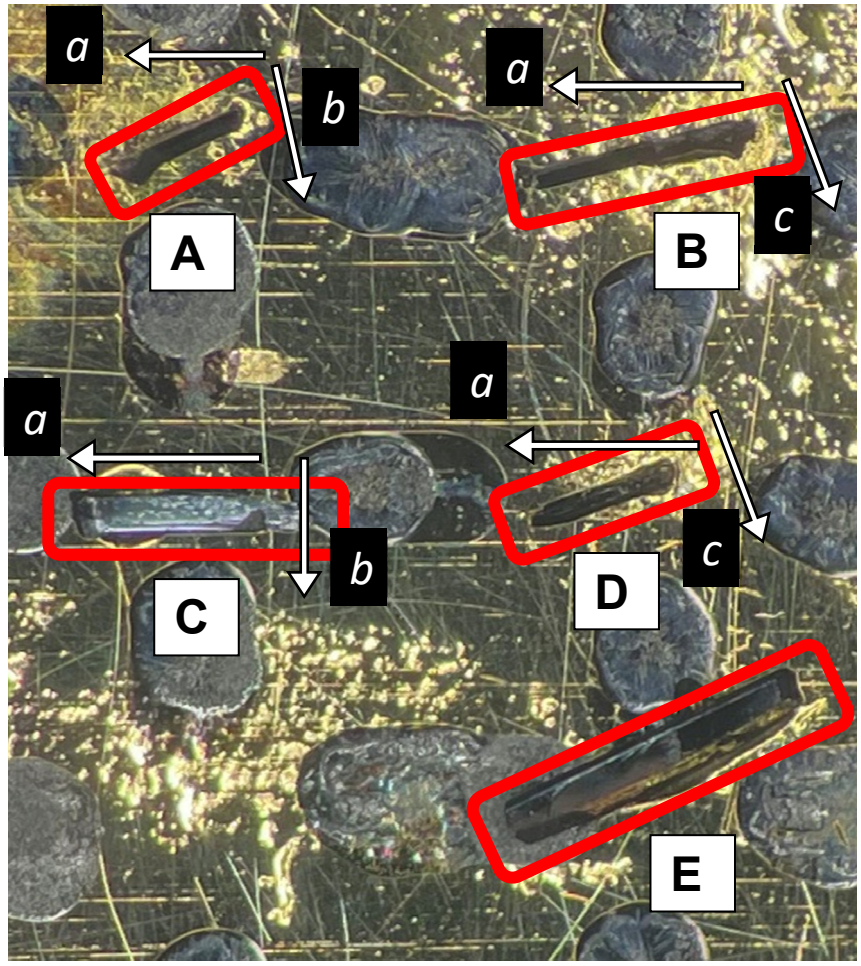

Figure S8. Sample setting in the cryostat for reflectance spectra measurements. Microscope photograph showing sample location: five single crystals of A—E, where A = #212, B = #225, C = #232, and D = #218 in the serial crystal number. Arrows marked with *a*, *b*, and *c* indicate the crystallographic axes of each single crystal. The crystallographic axes of crystal E were not known and not used in the measurements. The spectra in Figures 5a and 5b were measured using the single crystals A, while the spectra in Figure 5c were measured using the single crystal D.

Table S6. Best-fitting parameters obtained from the curve-fitting analysis of reflectance spectra.[a]

Polarisation	Temperature (K)	ε_c[b]	ω_p (cm^{-1})	τ^{-1} (cm^{-1})
E // ***a***	294	14.3	4364	1312
	250	21.6	5197	1050
	200	50.9	7688	785
	150	17.2	4612	886
	100	17.9	4946	810
	50	23.9	5615	940
	6.8	27.1	5808	1079
E //***a**** (*ab* plane)	294	14.7	4292	1119
	250	17.5	4714	975
	200	38.3	6910	803
	150	22.3	5203	889
	100	17.1	4797	819
	50	19.3	5057	911
	6.8	27.4	5892	1041
E //***a**** (*ac* plane)	294	17.1	3478	1215
	250	10.8	2882	1376
	200	28.7	3981	838
	150	15.0	3353	1204
	100	12.4	3223	1174
	50	11.2	3252	1292
	6.8	11.0	3380	1430

[a] The fitting function is a Drude model (Eq. S1).

$$R(\omega) = \frac{|\varepsilon(\omega)| + 1 - \sqrt{2\{|\varepsilon(\omega)| + \mathrm{Re}[\varepsilon(\omega)]\}}}{|\varepsilon(\omega)| + 1 + \sqrt{2\{|\varepsilon(\omega)| + \mathrm{Re}[\varepsilon(\omega)]\}}}$$

$$\varepsilon(\omega) = \varepsilon_c - \frac{\omega_p^2}{\omega\left(\omega + \frac{i}{\tau}\right)} \qquad \text{(Eq. S1)}$$

where

R: reflectance
ω : wavenumber
ε: dielectric function
ε_c: background dielectric constant ($\varepsilon_c \equiv \lim_{\omega\to\infty} \varepsilon(\omega)$)
ω_p : plasma frequency of intraband transition
τ: relaxation rate of free carriers
$i \equiv \sqrt{-1}$

[b] The fitting values of ε_c are unusually large because the reflectance beyond the Drude dispersion (≥ 1500 cm^{-1}) is nearly constant and unusually high appearing as if it is a high-level baseline. This is probably because continuum broad peaks should be underlying in this region, which is suggested by the fact that a dip characteristic to Drude dispersions is not observed at the Drude edge in any spectrum in **Figure S9**. Thus, the obtained values of ε_c require to be examined by independent methods. However, the values of ε_c do not affect the reliability of ω_p and τ.

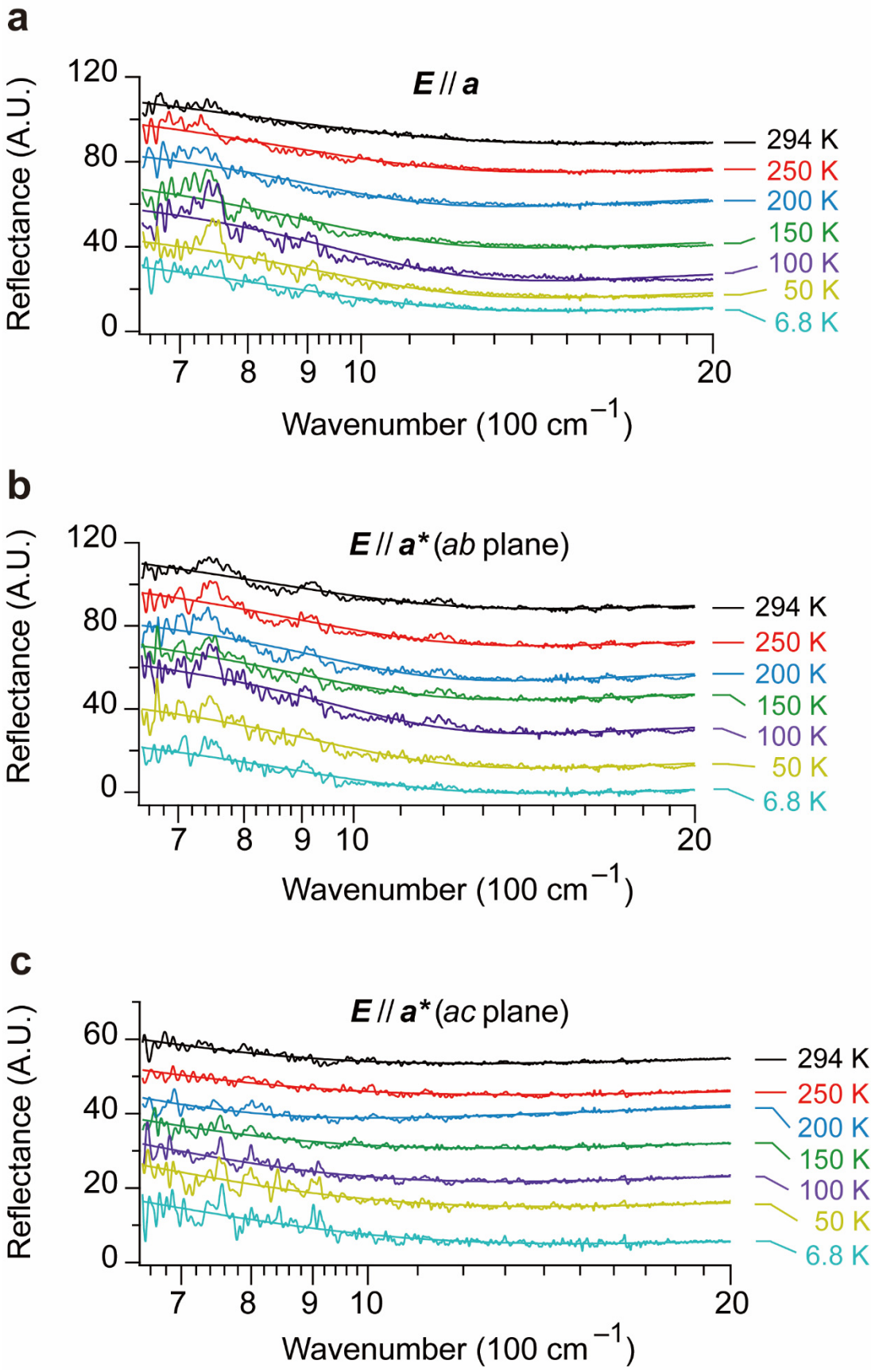

Figure S9. Observed and calculated reflectance spectra (close-up view of 650—2000 cm^{-1} based on the same data in **Figures 5b, 5d, and 5f**). The calculated spectra (smooth curves) are obtained by the curve-fitting analysis based on a Drude model (Eq. S1). The fitting parameters are shown in **Table S6**.

References

[S1] Y. Sasaki, M. Takase, S. Mori and H. Uno, *Molecules*, 2020, **25**, 2486.

[S2] M. Takase, V. Enkelman, D. Sebastiani, M. Baumgarten and K. Müllen, *Angew. Chem. Int. Ed.*, 2007, **46**, 5524—5527.

[S3] L. Pauling, Chapter 7, Table 7-20 and the related discussion, pp. 260—261, in "The Nature of the Chemical Bond," **1960**, Third Ed., Cornell University Press, Ithaca, New York, USA.

[S4] R. Oka, K. Ohara, K. Konishi, I. Yamane, T. Shimada and T. Naito, *Magnetochemistry*, 2023, **9**, 153.

[S5] K. Funatsu, R. Oka, N. Tajima and T. Naito, *Crystals*, 2023, **13**, 1606.

[S6] P. Hohenberg and W. Kohn, *Phys. Rev*., 1964, **136**, B864.

[S7] W. Kohn and L. J. Sham, *Phys. Rev.*, 1965, **140**, A1133.

[S8] D. M. Ceperley and B. J. Alder, *Phys. Rev. Lett.*, 1980, **45**, 566.

[S9] J. P. Perdew and A. Zunger, *Phys. Rev. B*, 1981, **23**, 5048.

[S10] D. Vanderbilt, *Phys. Rev. B*, 1990, **41**, 7892.

[S11] P. Giannozzil, *et al*., *J. Phys.: Condens. Matter*, 2009, **21**, 395502.

[S12] P. Deplano, F. A. Devillanova, J. R. Ferraro, M. L. Mercuri, V. Lippolis and E. F. Trogu, *Appl. Spectrosc.*, 1994, **48**, 1236—1241.

[S13] R. Oka, K. Ohara, N. Tajima, T. Shimada and T. Naito, *Mater. Adv.*, 2024, **5**, 1492—1501.